A Study of Timing Resolutions on Particle Identification in the Hall D Dectector at Jefferson Lab

Curtis A. Meyer

March 1, 1999

1 Introduction

In order to examine the response of the Hall D stage I detector, we have employed the MCFast Monte Carlo program to simulate the detector system as shown in Figure 1. Particles are tracked through the detector, and then a reconstruction with suitable errors is performed within the code. In addition, the time–of–flight information is recorded in two systems. The *central* comes from the first layers of the Pb–SciFi calorimeter, while the *forward* comes from a plane of scintillators directly in front of the Pb–glass array. In order to construct the *mass* of the particle, it is necessary to measure both p and v. The former comes from the reconstructed particle, while the latter requires knowledge of both the flight path length, **L**, and the time–of–flight from the start counter to the detector plane, **t**. Using these in equation 1, we are able to reconstruct the mass of the particle.

$$m = p\sqrt{\frac{1}{(L/ct)^2} - 1} \tag{1}$$

The particular reaction studied is $\gamma p \rightarrow K^+K^-\pi^+\pi^-p$ where the four–meson system comes from a $1.7GeV/c^2$ mass resonance of width $0.250GeV/c^2$. The reaction has been generated for incident photon energies of 6, 8, 10 and 12 GeV using the GENR8 generator program with a t–slope of 5. The main purpose of this study is to understand how well we will be able to separate kaons from pions and protons. During all of this, it should be kept in mind that the total rate of kaon production will be down by at least 2 orders of magnitude from the pion production.

To establish a baseline, Figures 2 and 3 show the reconstructed masses for *perfect* timing and path length measurements. The smearing here arises from the uncertainty in the particle's reconstructed momentum only. In section 2 we will examine the effects of smearing the time of flight on these. One striking effect is the rapid deterioration of these spectra, even with 50 ps time resolution. In section 3 we will perform the same study by varying the path length. While this effect is not as significant as the timing smearing, it is not safe to neglect it in the design of the detector.

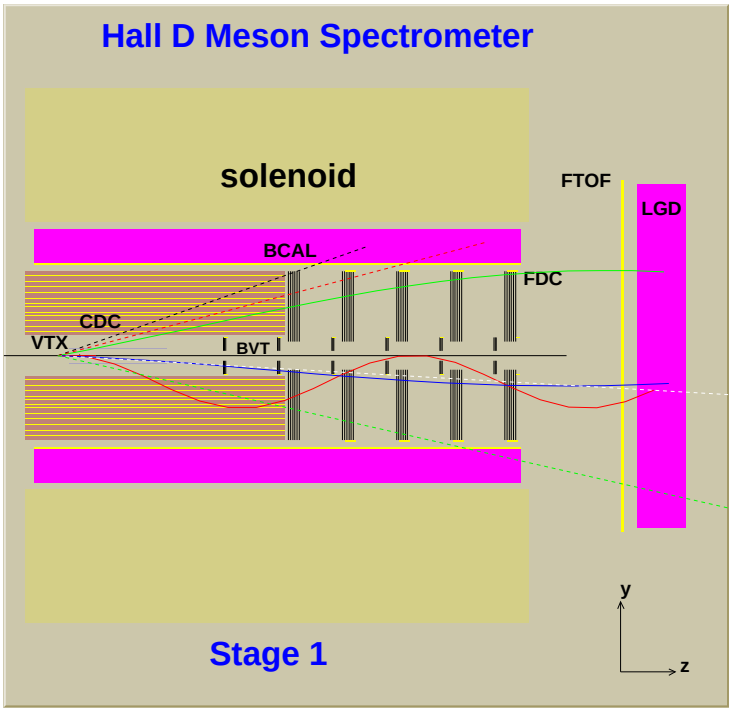

Figure 1: The Hall D Stage I detector. The central time–of–flight system is at the inside surface of the BCAL, while the forward time–of–flight system is labeled at FTOF. The event shown has both charged particles and photons in it.

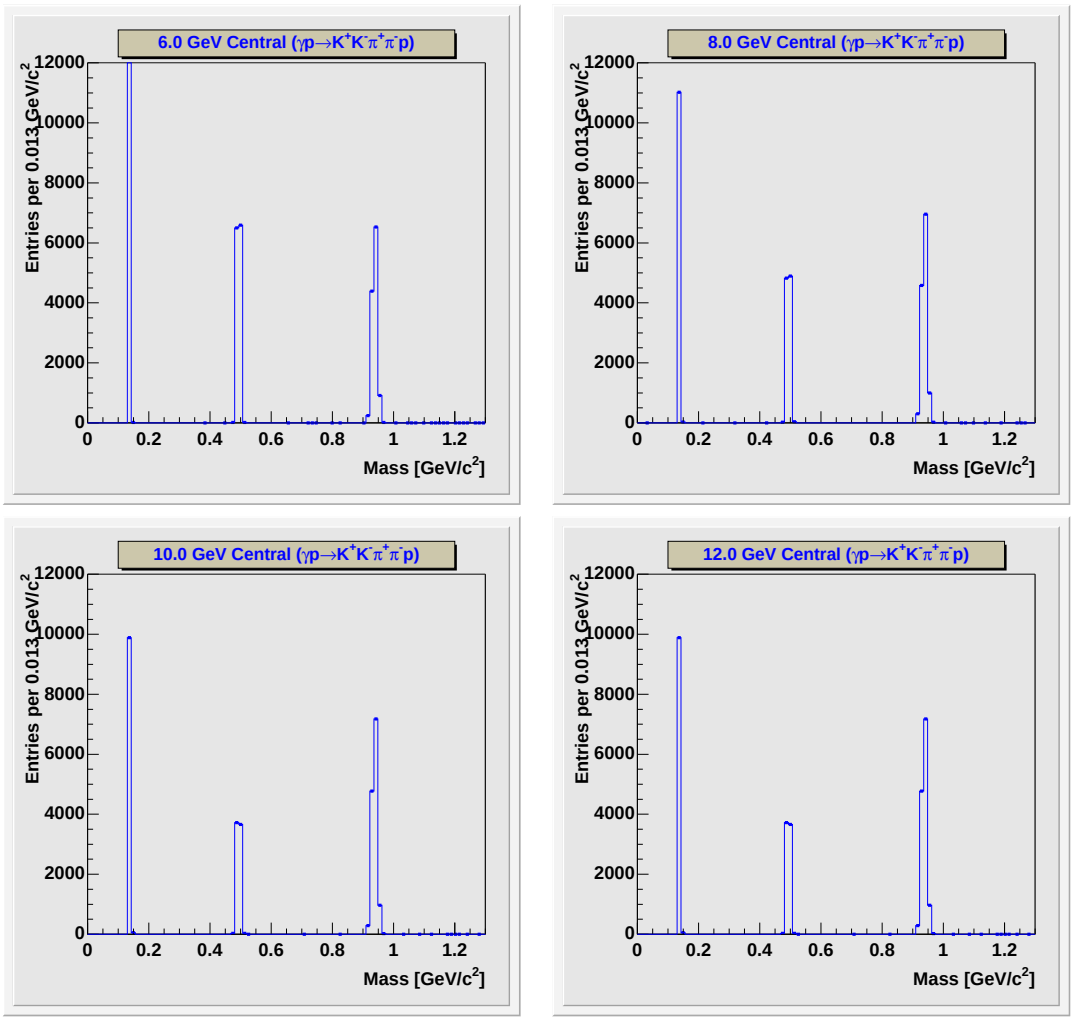

Figure 2: The reconstructed mass for perfect timing resolution in the central region. The reaction is for $\gamma p \rightarrow K^+K^-\pi^+\pi^-p$. The figures are for four different incident photon energies, $6.0GeV$, $8.0GeV$, $10.0GeV$ and $12.0GeV$.

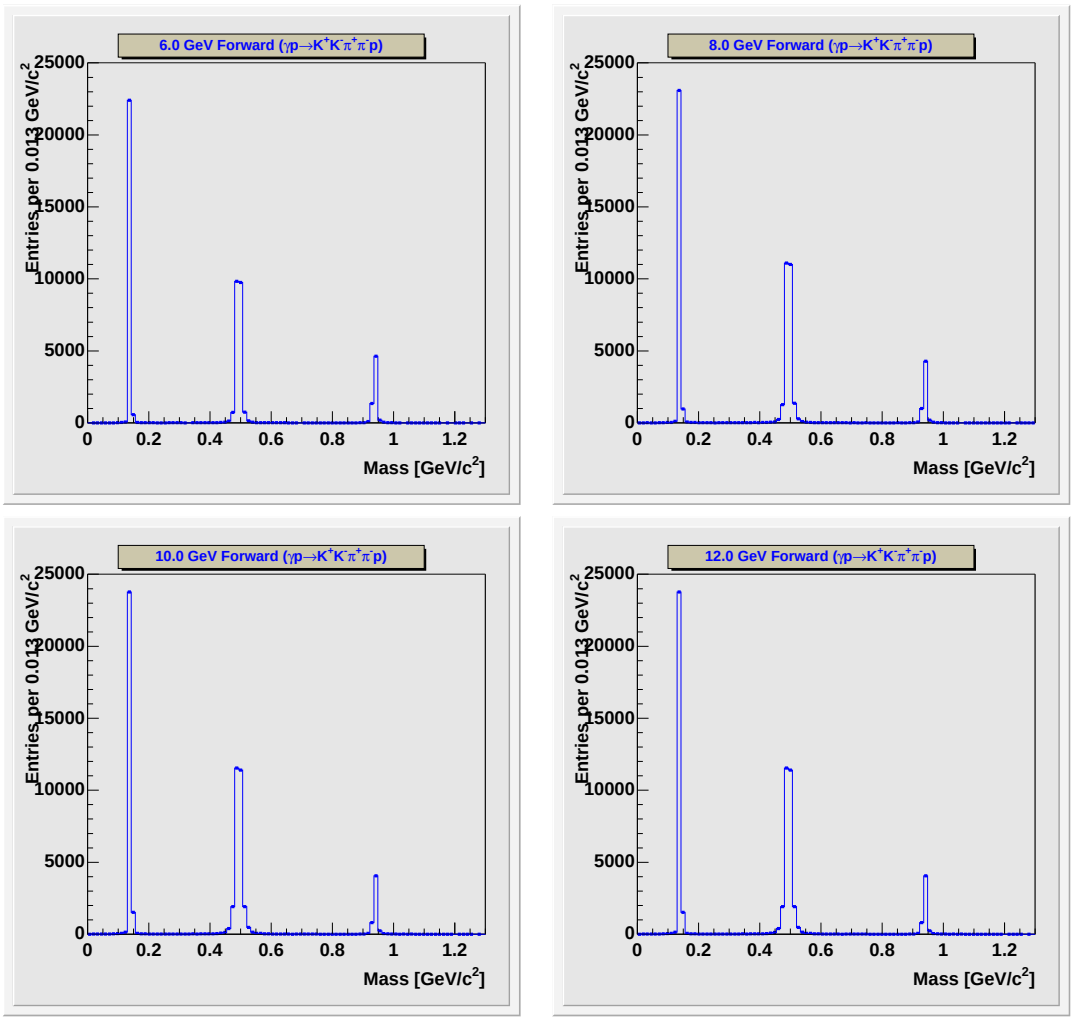

Figure 3: The reconstructed mass for perfect timing resolution in the forward region. The reaction is for $\gamma p \rightarrow K^+K^-\pi^+\pi^-p$. The figures are for four different incident photon energies, $6.0GeV$, $8.0GeV$, $10.0GeV$ and $12.0GeV$.

2 Time of flight Resolution

In order to study the effect of timing resolution on the reconstructed mass, we have smeared the measured time–of–flight, **t**, in equation 1. The exact form of the smearing is the addition of Gaussian distributed offset whose mean value is 0 and whose σ varies from $50ps$ up to $2ns$. Figures 5 and 7 show the effect of this smearing on the reconstructed mass. The error in reconstructed mass as a function of the error in time can be derived from equation 2 as given in equation 3. The non–linear response in $\frac{\Delta m}{m}$ to $\frac{\Delta t}{t}$ implies that a Gaussian distortion in time will lead to a non–Gaussian distortion in mass. This is in fact seen, with a Gaussian function giving a poor fit to the resulting mass distributions.

$$\frac{\partial m}{\partial t} = \frac{m}{t(1-(L/ct)^2)} \tag{2}$$

$$\frac{\Delta m}{m} = \frac{\Delta t}{t(1-(L/ct)^2)} \tag{3}$$

Figure 4 shows the total time–of–flight of all particles detected in the central region of the detector broken up by particle type. Smearing these times leads to the mass distributions seen in Figure 5 for the central detector. Figure 6 shows the time–of–flight distributions for all particles seen in the forward system. Smearing these times yields the mass distributions seen in Figure 7 in the forward system. These plots show the resulting mass distributions for the time–of–flight σ's ranging from 50 ps up to 2 ns. It should be noted that the 50 ps has already significantly deteriorated from the perfect resolution as given in Figures 2 and 3. It is also interesting that the kaon distribution is deteriorating faster than either the pion or the proton. The problem appears to be mostly kaons not being identified as kaons, rather than pions or protons being misidentifies as kaons.

In order to quantify the previous statements, we have defined a kaon–window in reconstructed mass. All particles that have a reconstructed mass between $0.400GeV/c^2$ and $0.600GeV/c^2$ are identified as a kaon. We have then repeated the smearing exercise and counted the fraction of all pions, kaons and protons that are so identified. These fractions are plotted in Figure 8 for the central region, and in Figure 9 in the forward region. These plots clearly show the rapid deterioration in the kaon identification as the time–of–flight resolutions gets worse. A time resolution of 200 ps (1σ), roughly what CLAS currently has, means that the central region correctly identifies only 60% of the kaons at $E_\gamma = 6$ GeV and only 48% at $E_\gamma = 12$ GeV. The behavior of the forward region is seen to be slightly better. In addition, it becomes clear that pions are far more likely than protons to be misidentified as a kaon. At 200 ps resolution in the central region, 5% of the pions are identified as kaons at $E_\gamma = 6$ GeV. This has increased to about 15% at $E_\gamma = 12$ GeV.

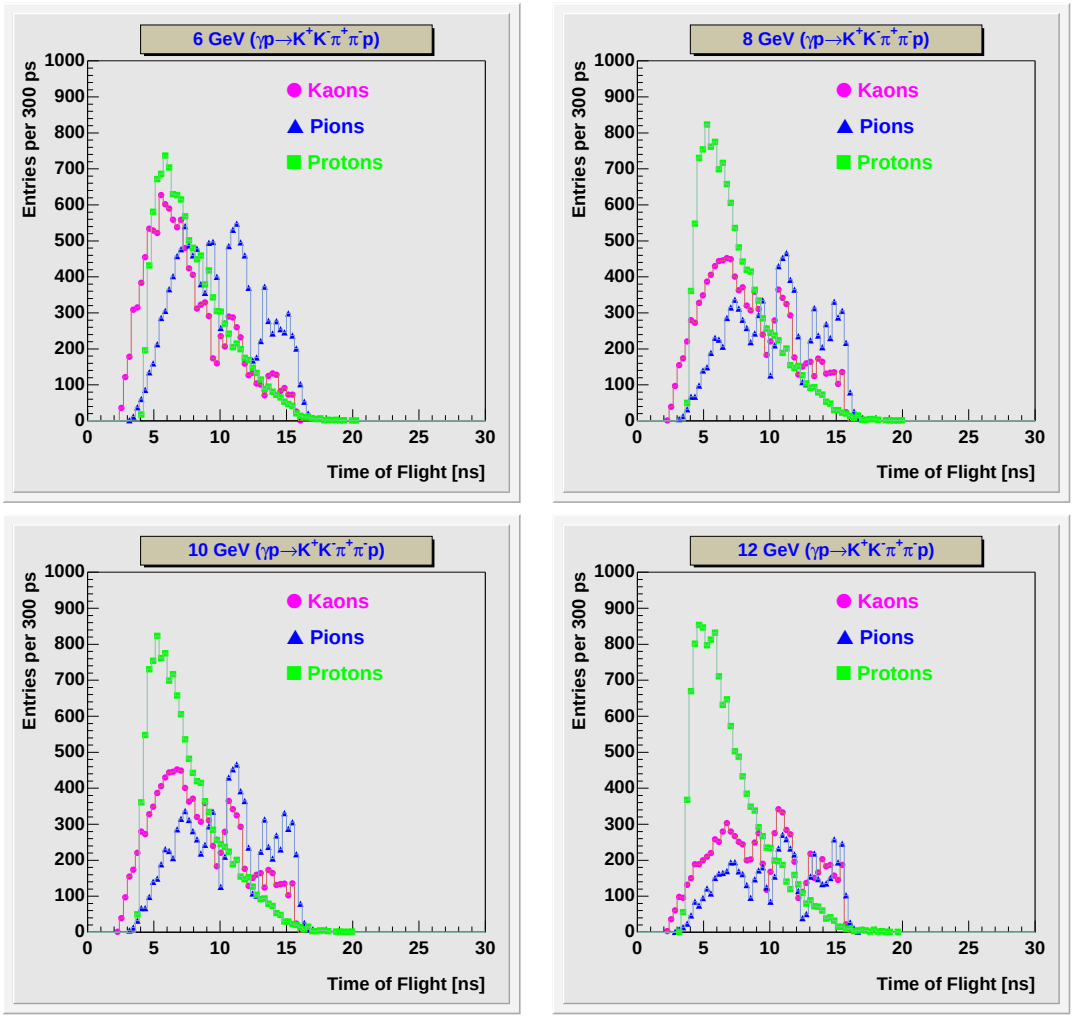

Figure 4: The time–of–flight of all particles in the central region. The particles come from the reaction $\gamma p \to K^+K^-\pi^+\pi^-p$. The figures are for four different incident photon energies, $6.0GeV$, $8.0GeV$, $10.0GeV$ and $12.0GeV$.

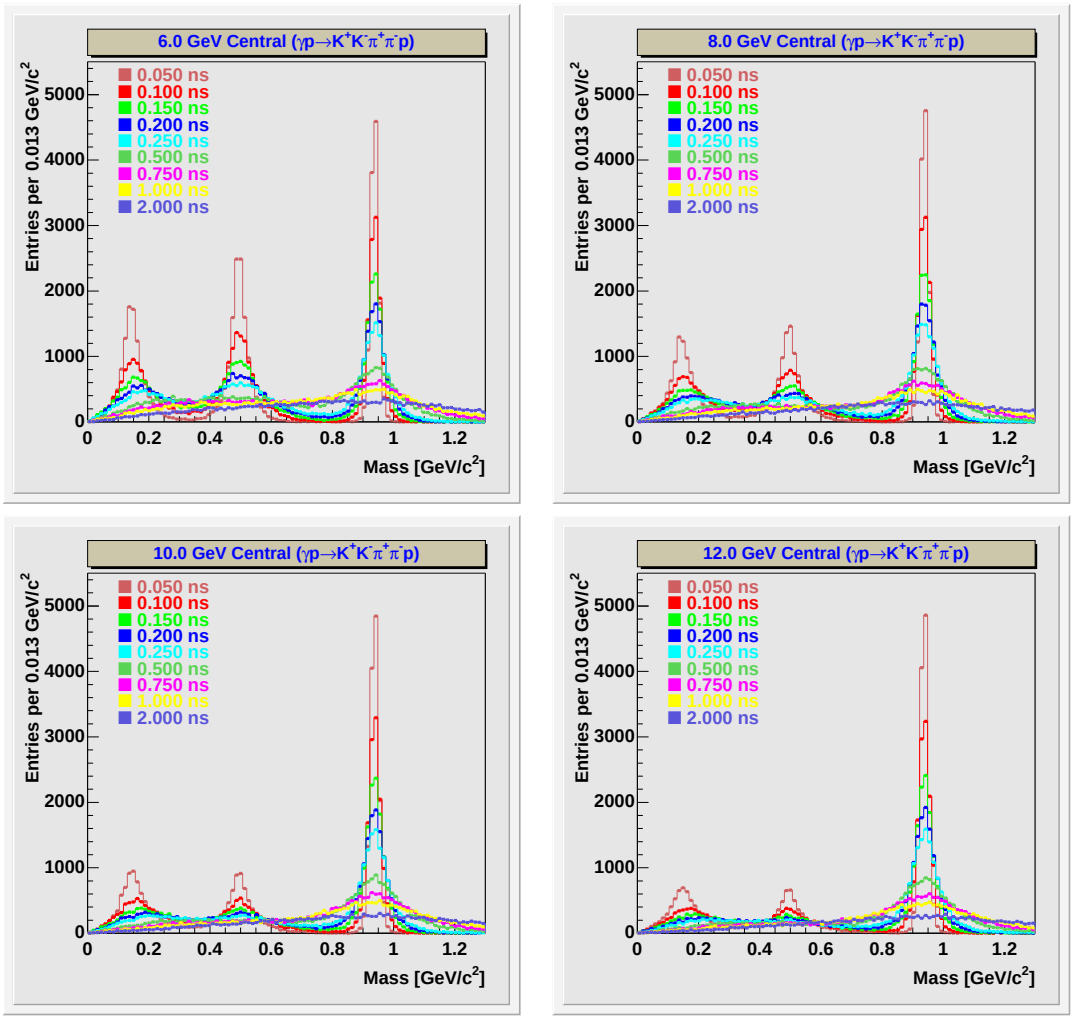

Figure 5: The reconstructed mass as a function of timing resolution in the central region. The reaction is for $\gamma p \rightarrow K^+K^-\pi^+\pi^-p$. The figures are for four different incident photon energies, $6.0GeV$, $8.0GeV$, $10.0GeV$ and $12.0GeV$.

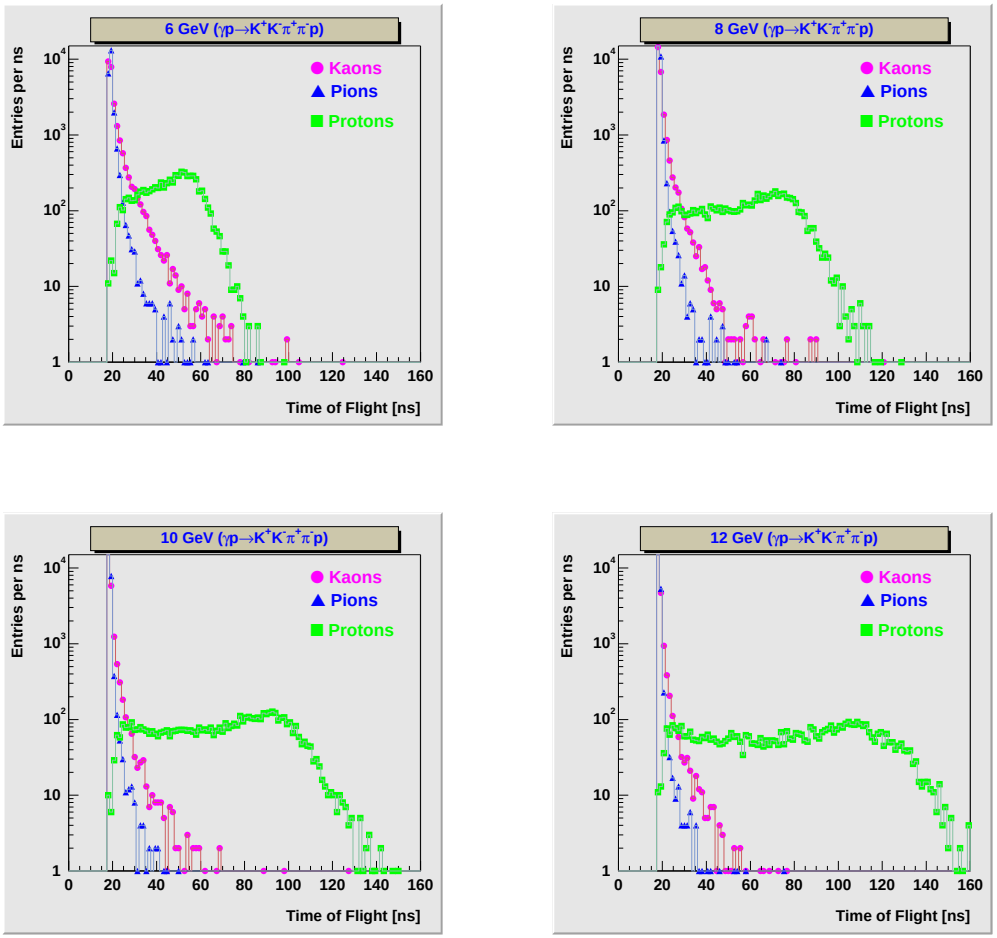

Figure 6: The time–of–flight of all particles in the forward region. The particles come from the reaction $\gamma p \to K^+K^-\pi^+\pi^-p$. The figures are for four different incident photon energies, $6.0GeV$, $8.0GeV$, $10.0GeV$ and $12.0GeV$.

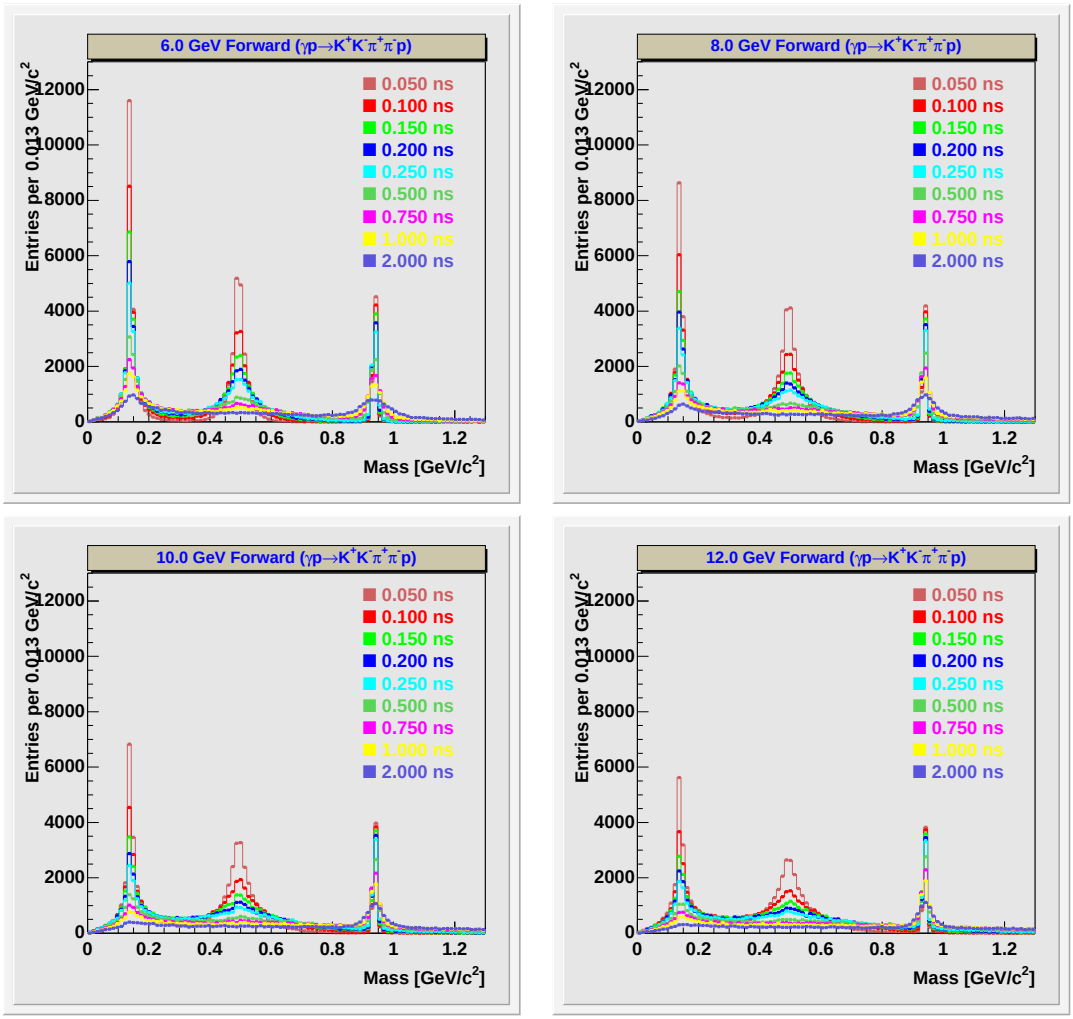

Figure 7: The reconstructed mass as a function of timing resolution in the forward region. The reaction is for $\gamma p \rightarrow K^+K^-\pi^+\pi^-p$. The figures are for four different incident photon energies, $6.0GeV$, $8.0GeV$, $10.0GeV$ and $12.0GeV$.

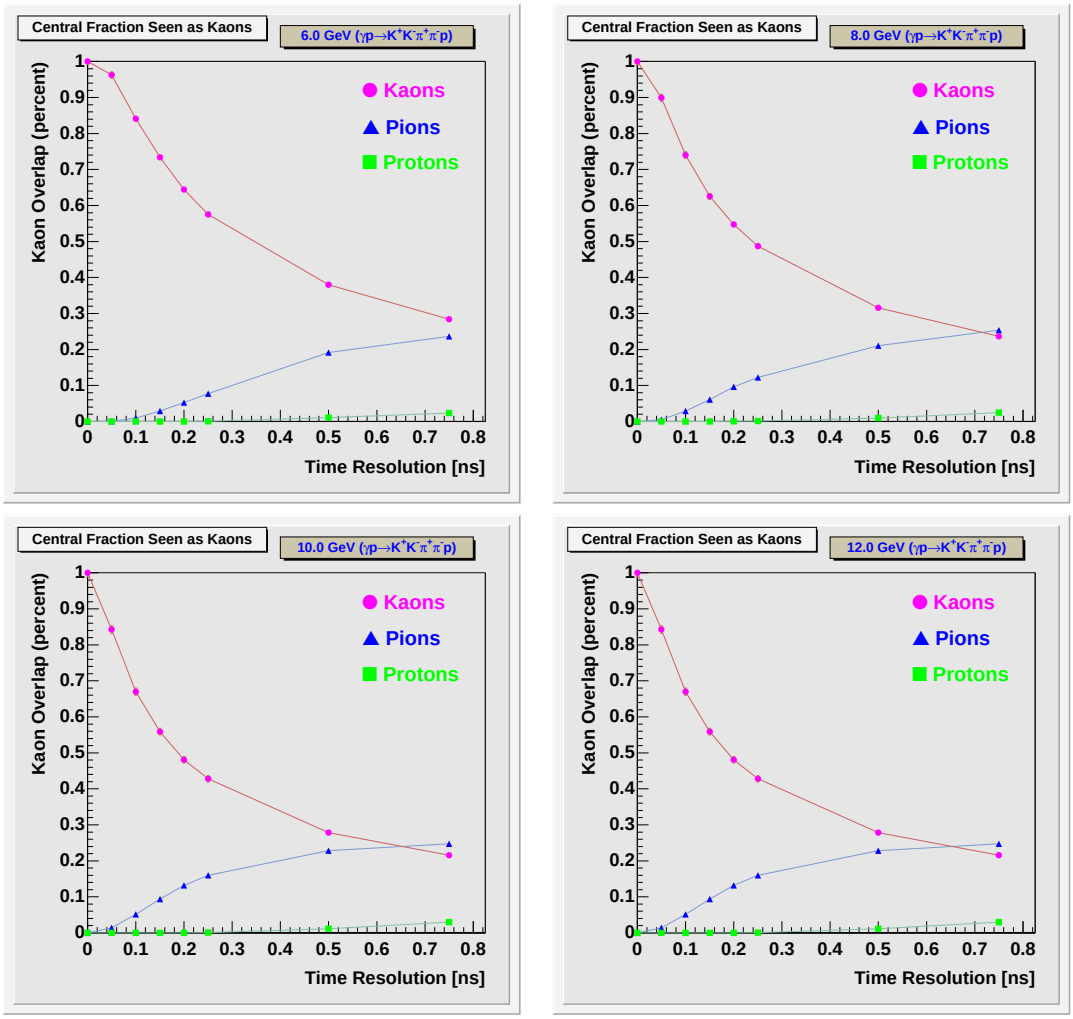

Figure 8: The fraction of K's, π's and p's which have a reconstructed mass inside a K window from $0.4GeV/c^2$ to $0.6GeV/c^2$. The plots are as a function of timing resolution in the central region. The reaction is for $\gamma p \to K^+K^-\pi^+\pi^-p$. The figures are for four different incident photon energies, $6.0GeV$, $8.0GeV$, $10.0GeV$ and $12.0GeV$.

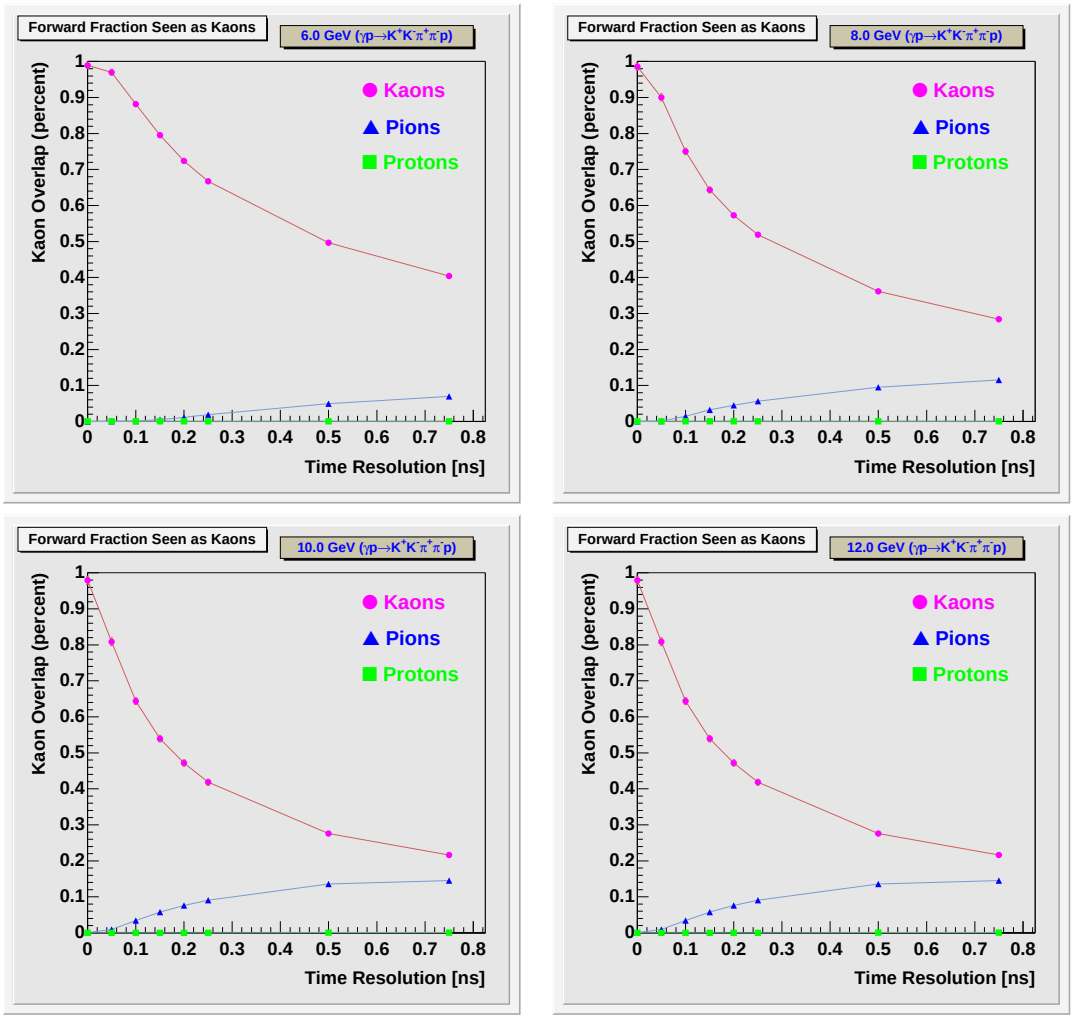

Figure 9: The fraction of K's, π's and p's which have a reconstructed mass inside a K window from $0.4GeV/c^2$ to $0.6GeV/c^2$. The plots are as a function of timing resolution in the forward region. The reaction is for $\gamma p \to K^+K^-\pi^+\pi^-p$. The figures are for four different incident photon energies, $6.0GeV$, $8.0GeV$, $10.0GeV$ and $12.0GeV$.

3 Path Length Resolution

In addition to the timing resolution examined in section 2, the path length of the reconstructed particle will also be uncertain. Part of this will arise due to uncertainties in the reconstructed momentum. However, in the central region the penetration depth of the charged particle in the scintillator may lead to smearing of the resolution. In order to try and simulate this, we have taken the nominal path length and added to it a Gaussian distributed distortion which ranges from 1 mm up to 5 cm. This offset is independent of the measured path length of the track. Equation 4 is used to find the error in reconstructed mass as a function of path length. This is given in equation 5. The form of the path length dependence is quite similar to that for time–of–flight as given in equation 3

$$\frac{\partial m}{\partial L} = \frac{-m}{L(1-(L/ct)^2)} \tag{4}$$

$$\frac{\Delta m}{m} = \frac{-\Delta t}{L(1-(L/ct)^2)} \tag{5}$$

Figure 10 shows the path length of all particles measured in the central time–of–flight system. Distorting these path lengths yields the mass distributions seen in Figure 11. Figure 12 shows distribution for particles detected in the forward region. Figure 13 shows the resulting mass distributions when the forward lengths are smeared. At least for the sizes of smearing adopted in in this study, the effect of length smearing is quite a bit smaller than that due to time smearing. As before, we can ask what fraction of kaons, pions and protons are identified as kaons due to the length smearing. These are shown in Figure 14 for the central region and Figure 15 for the forward region. These plots show far less overlap than that seen for the time smearing.

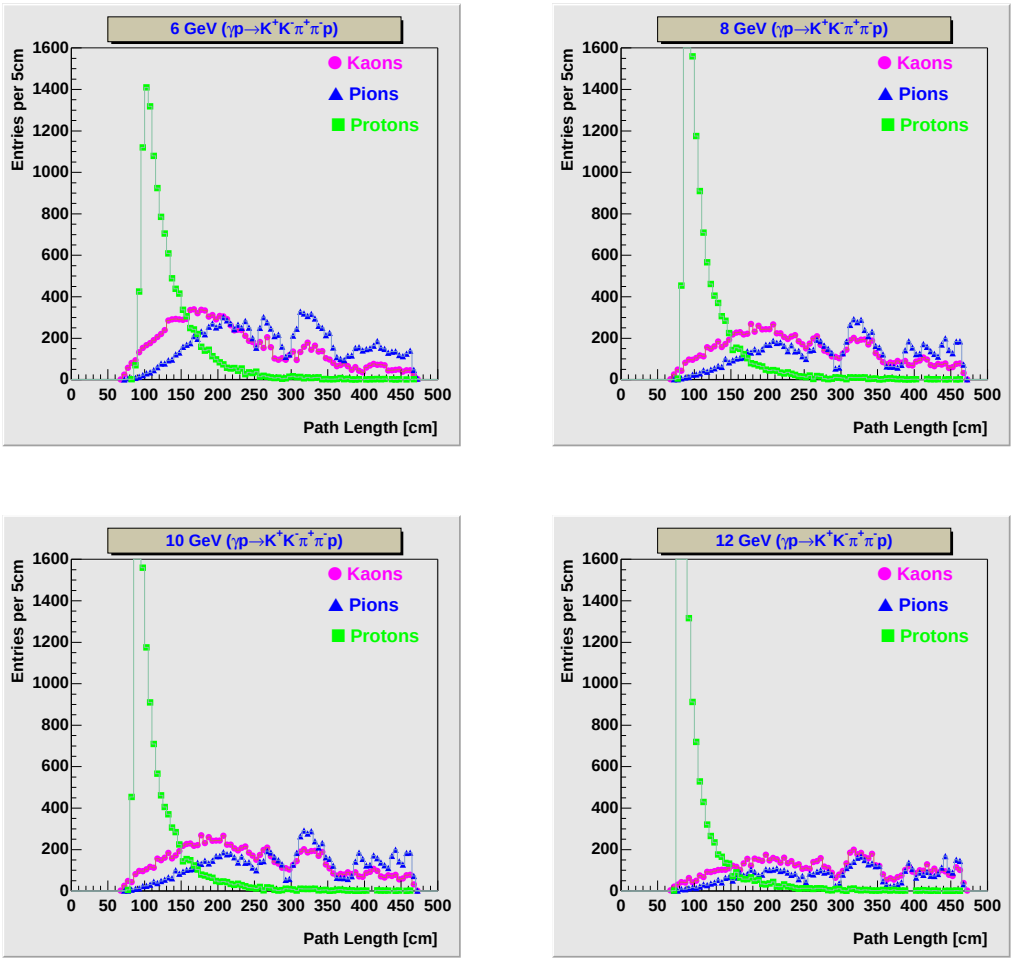

Figure 10: The path length of all particles in the central region. The particles come from the reaction $\gamma p \to K^+K^-\pi^+\pi^-p$. The figures are for four different incident photon energies, $6.0GeV$, $8.0GeV$, $10.0GeV$ and $12.0GeV$.

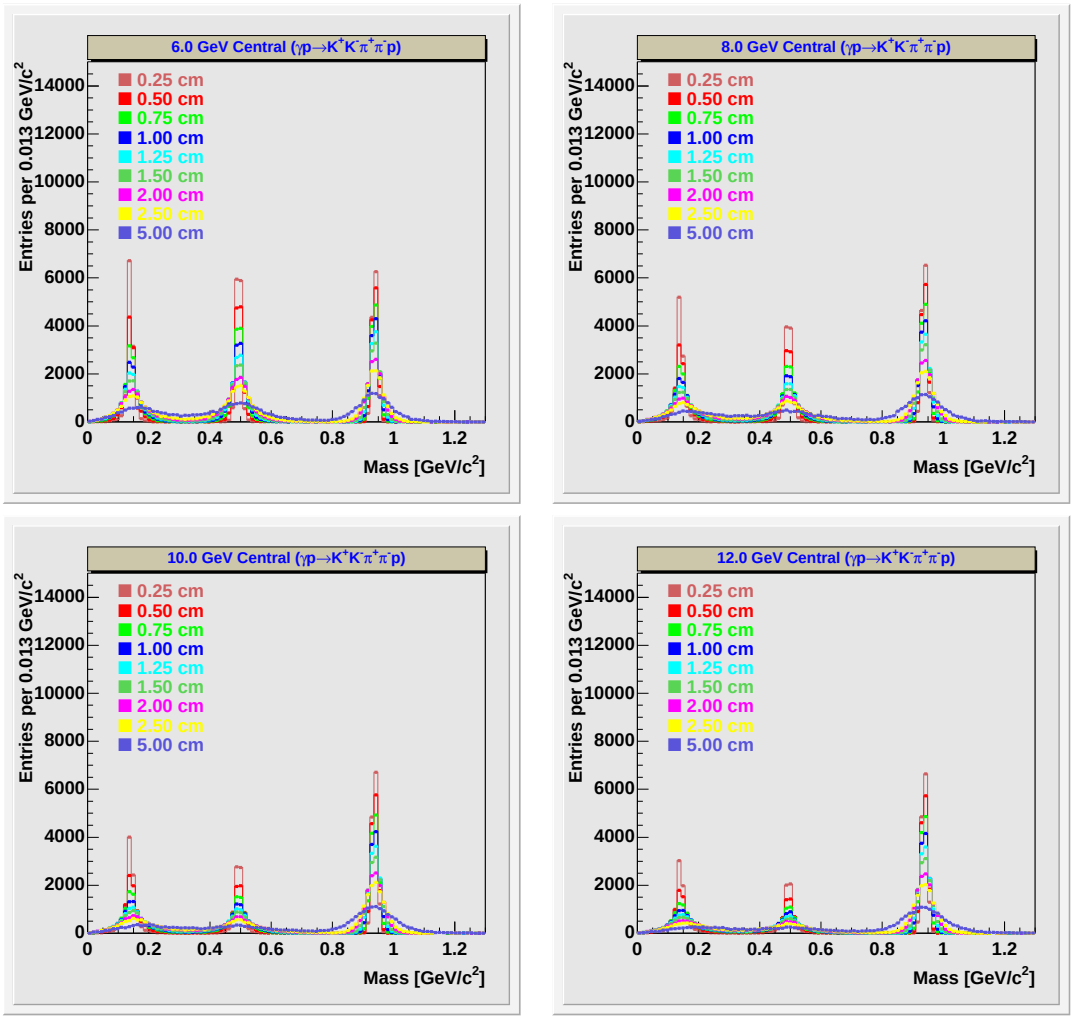

Figure 11: The reconstructed mass as a function of path length resolution in the central region. The reaction is for $\gamma p \to K^+K^-\pi^+\pi^-p$. The figures are for four different incident photon energies, $6.0GeV$, $8.0GeV$, $10.0GeV$ and $12.0GeV$.

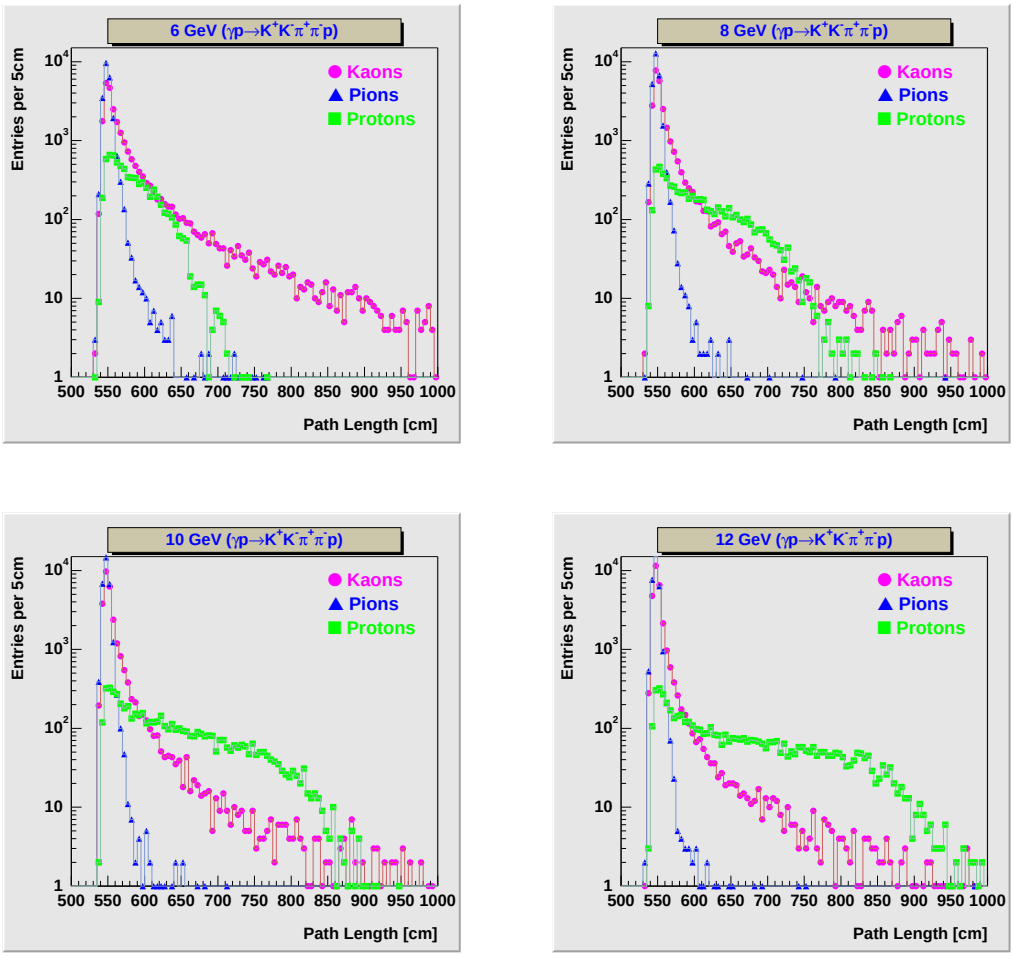

Figure 12: The path length of all particles in the central region. The particles come from the reaction $\gamma p \to K^+ K^- \pi^+ \pi^- p$. The figures are for four different incident photon energies, $6.0GeV$, $8.0GeV$, $10.0GeV$ and $12.0GeV$.

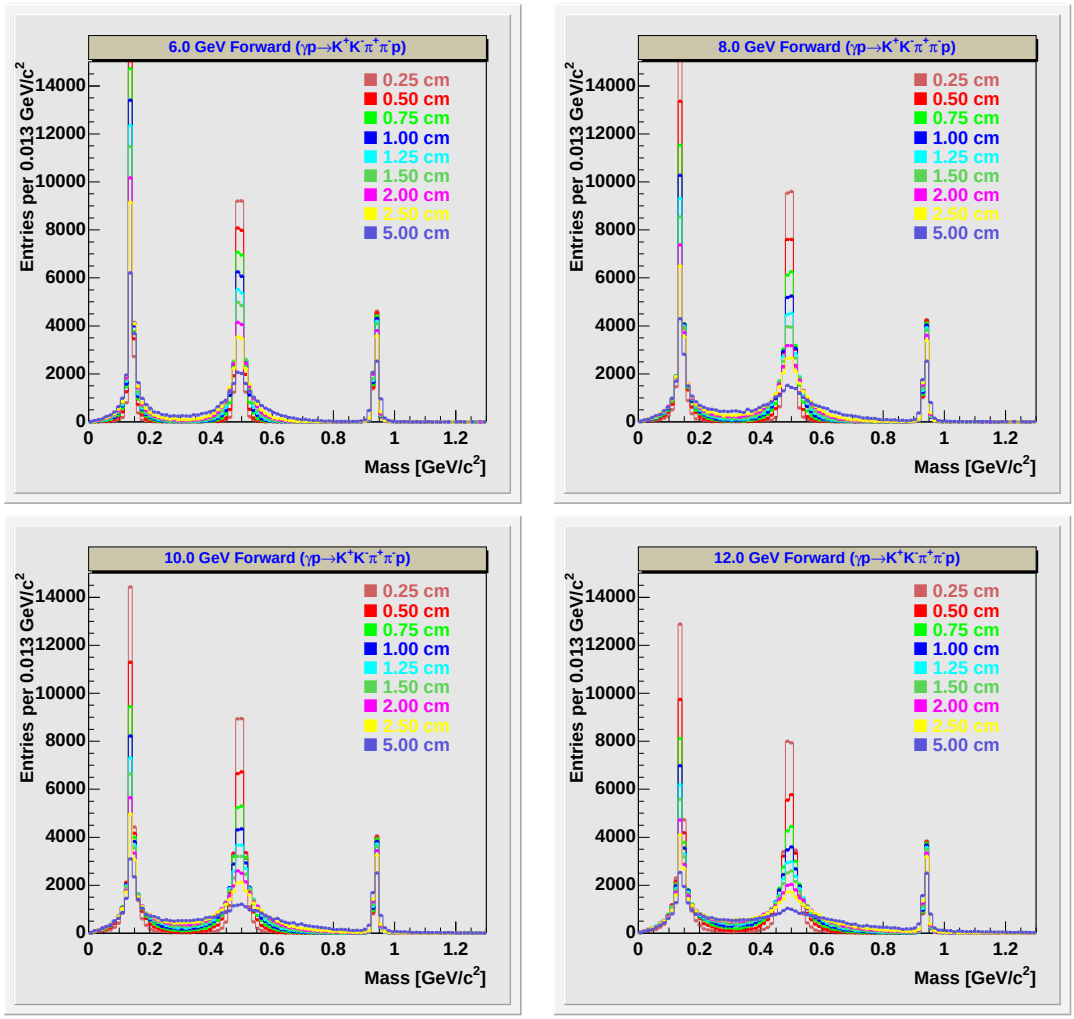

Figure 13: The reconstructed mass as a function of path length resolution in the forward region. The reaction is for $\gamma p \to K^+K^-\pi^+\pi^-p$. The figures are for four different incident photon energies, $6.0GeV$, $8.0GeV$, $10.0GeV$ and $12.0GeV$.

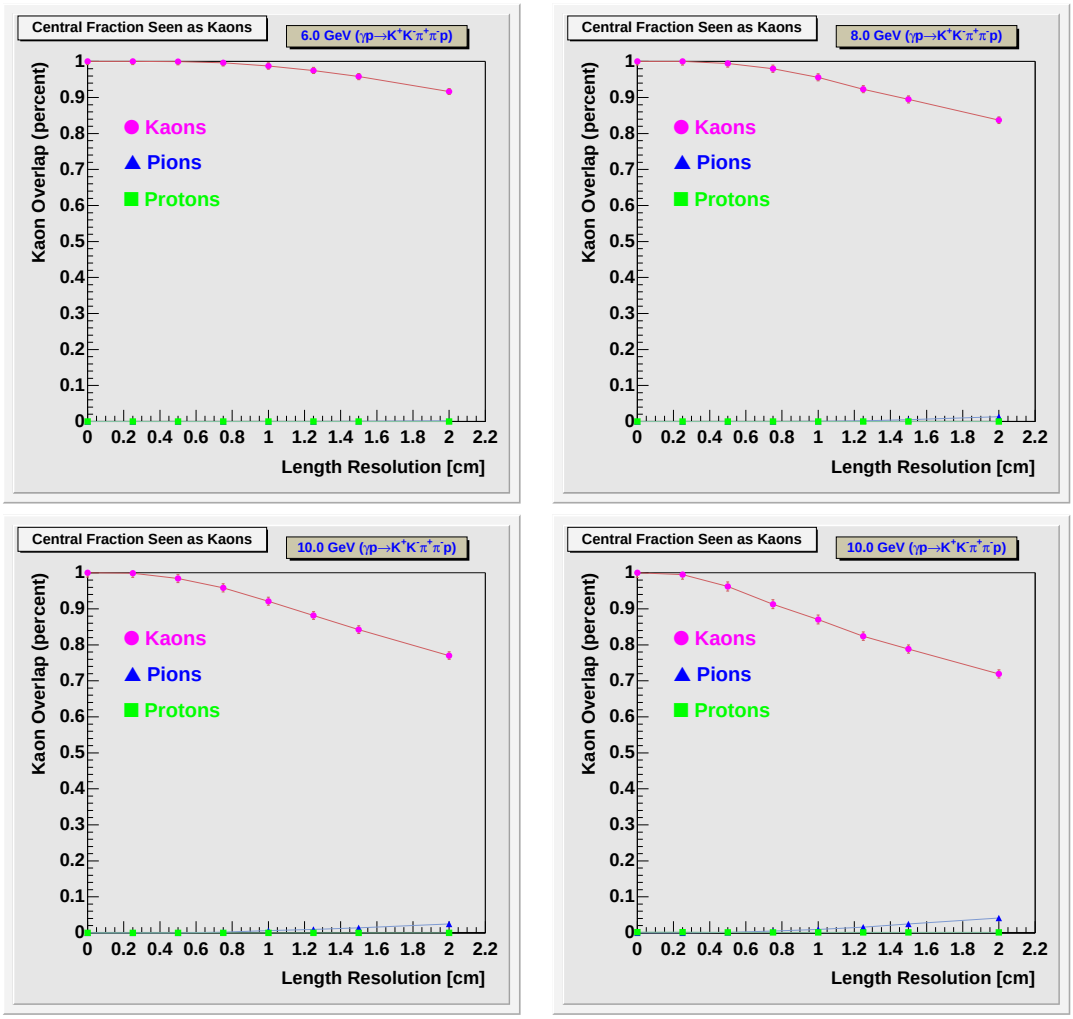

Figure 14: The fraction of K's, π's and p's which have a reconstructed mass inside a K window from $0.4GeV/c^2$ to $0.6GeV/c^2$. The plots are as a function of path length resolution in the central region. The reaction is for $\gamma p \rightarrow K^+K^-\pi^+\pi^-p$. The figures are for four different incident photon energies, $6.0GeV$, $8.0GeV$, $10.0GeV$ and $12.0GeV$.

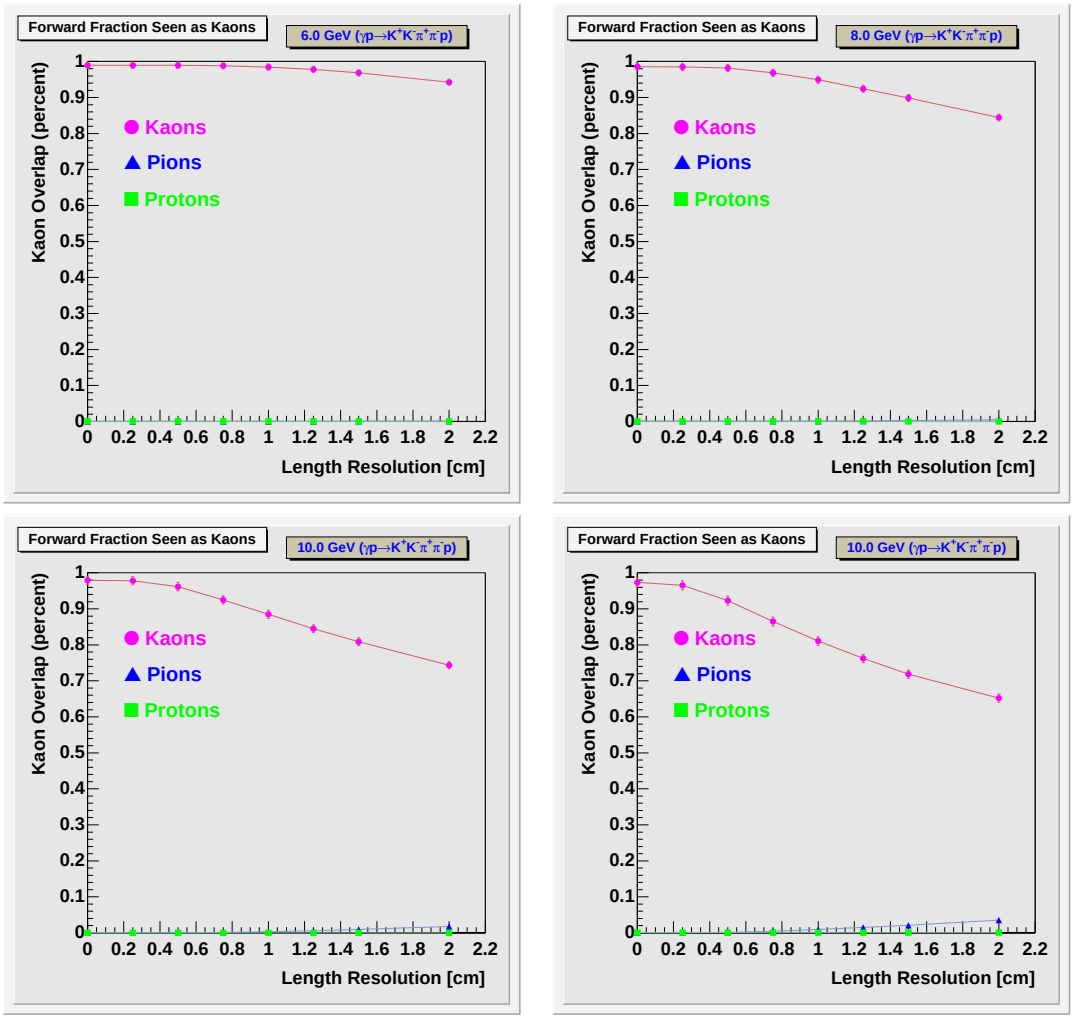

Figure 15: The fraction of K's, π's and p's which have a reconstructed mass inside a K window from $0.4GeV/c^2$ to $0.6GeV/c^2$. The plots are as a function of path length resolution in the forward region. The reaction is for $\gamma p \rightarrow K^+K^-\pi^+\pi^-p$. The figures are for four different incident photon energies, 6.0 GeV, 8.0 GeV, 10.0 GeV and 12.0 GeV.

4 Summary and Conclusions

This report has studied the reaction $\gamma p \rightarrow K^+K^-\pi^+\pi^-p$ for 6.0 GeV, 8.0 GeV, 10.0 GeV and 12.0 GeV incident photon energies. While this particular reaction may not be typical of all reactions where K/π separation is important, it should be reasonably representative of them. It also does not account for the fact that the forward system will also involve a Čerenkov detector system as higher energies are reached. The most significant plots in this report are Figures 8, 9, 14 and 15. These indicate that for most reasonable time–of-flight resolutions, the separation problem is not one of pions and protons being identified as kaons, but rather is one of kaons not being identified as kaons. This is particularly extreme in the central region where a 200 ps 1σ resolution at 12 GeV leads to over 50% of the kaons **not** being identified as kaons. Some of these probelems will be allevieated by dE/dx in the central region. However, K/π separtion with dE/dx is usually only good for momenta up to about $0.6 GeV/c$. The bottom line is that with only the current systems, we are likely to have difficulty identifying kaons at the highest beam energies in the central detector system. We may need to consider additional particle detection systems in the central region.